

# Influence of Defects on the Schottky Barrier Height at BaTiO<sub>3</sub>/RuO<sub>2</sub> Interfaces

Katharina N. S. Schuldt, Hui Ding, Jean-Christophe Jaud, Jurij Koruza, and Andreas Klein\*

The Schottky barrier formation between polycrystalline acceptor-doped BaTiO<sub>3</sub> and high work function RuO<sub>2</sub> is studied using photoelectron spectroscopy. Schottky barrier heights for electrons of  $\approx 1.4$  eV are determined, independent of doping level and oxygen vacancy concentration of the substrates. The insensitivity of the barrier height is related to the high permittivity of BaTiO<sub>3</sub>, which results in space-charge regions (SCRs) being considerably wider than the inelastic mean free path of the photoelectrons. SCRs at any kind of interface should, therefore, be more important for the electronic and ionic conductivities in BaTiO<sub>3</sub> than in materials with lower permittivity. A Ba-rich phase at the surface of reduced acceptor-doped BaTiO<sub>3</sub> is also identified, which is explained by the formation of Ti vacancies in the 2D electron gas region at the surface.


## 1. Introduction

The progress toward smaller, lighter, and ubiquitous electronic devices reveals new requirements for electronic compounds. In the case of multilayer ceramic capacitors (MLCCs), the downscaling of the capacitor's dielectric thickness with constant dielectric field leads to an increasing field stress.<sup>[1]</sup> Resistance degradation, which is a characteristic feature and major restriction of,

K. N. S. Schuldt, H. Ding, Prof. A. Klein  
Department of Materials and Earth Sciences  
Electronic Structure of Materials  
Technical University of Darmstadt  
Otto-Berndt-Str. 3, 64287 Darmstadt, Germany  
E-mail: aklein@esm.tu-darmstadt.de

J.-C. Jaud  
Department of Materials and Earth Sciences  
Structure Research  
Technical University of Darmstadt  
Alarich-Weiss-Str. 2, 64287 Darmstadt, Germany

Dr. J. Koruza  
Department of Materials and Earth Sciences  
Nonmetallic Inorganic Materials  
Technical University of Darmstadt  
Alarich-Weiss-Str. 2, 64287 Darmstadt, Germany

 The ORCID identification number(s) for the author(s) of this article can be found under <https://doi.org/10.1002/pssa.202100143>.

© 2021 The Authors. physica status solidi (a) applications and materials science published by Wiley-VCH GmbH. This is an open access article under the terms of the Creative Commons Attribution-NonCommercial License, which permits use, distribution and reproduction in any medium, provided the original work is properly cited and is not used for commercial purposes.

DOI: 10.1002/pssa.202100143

nowadays, BaTiO<sub>3</sub>-based ceramic capacitors and which can be traced back to the field-driven migration of oxygen vacancies, is, therefore, intensively studied.<sup>[1–8]</sup>

The overall content of oxygen vacancies in the dielectric, which determines the overall conductivity and degradation behavior, will change if oxygen is exchanged at the electrode interfaces.<sup>[4,6]</sup> It has been reported that, at high temperature and electric fields, O<sub>2</sub> bubbles are forming under Pt anodes during degradation.<sup>[6]</sup> On the other hand, it has been shown that oxygen exchange is affected by ionic space-charge regions (SCRs),<sup>[9,10]</sup> which develop in the presence of electrostatic potential differences if ionic defects are mobile.<sup>[11]</sup> Understanding the formation of SCRs in oxide dielectrics is, therefore, of particular importance.

An ideal test case for the formation of SCRs is Schottky barriers, where the Fermi level at the surface/interface can be changed by deposition of materials with different work functions. If this deposition is performed at room temperature, where ionic defects in BaTiO<sub>3</sub> are immobile,<sup>[12,13]</sup> this will leave the Fermi level in the bulk unchanged. On the other hand, the Fermi level in the bulk can be changed by pretreatment of the substrate in different atmospheres.

A substantial variation of barrier formation and evolution of space-charge potential on the bulk defect concentration have been identified for SrTiO<sub>3</sub>, ZnO, Cu<sub>2</sub>O, and other materials.<sup>[14–18]</sup> The reason for the observed dependence on defect concentration is closely related to the strategy for the manipulation of energy band alignment and barrier heights in semiconductor junctions, where high doping concentrations are used to shrink the width of SCRs to enable carrier tunneling.<sup>[19]</sup> The observation of defect-related barrier modification by photoelectron spectroscopy (PES) is possible, as the inelastic mean free path of the photoelectrons in typical experiments is in the range of 13 nm,<sup>[20]</sup> which is comparable to the tunneling distance of electrons. If the SCR is of comparable extension, the binding energies measured by PES do no longer reflect the Fermi-level position directly at the interface.<sup>[14,21]</sup> For extreme defect concentrations, the width of SCRs can become less than 1 nm. In this case, PES binding energies might reveal a Fermi energy close to that in bulk of the material.<sup>[22]</sup> In this respect, PES might also be used to reveal the energy levels of defects in the bandgap. If the Fermi level will cross the defect's energy level in a space region, the charge density will change (increase) abruptly and form a very

very

narrow SCR toward the interface. For high defect concentrations, PES will eventually probe the Fermi-level position at which the crossing with defect level occurs. Such effects have been reported for ZnO,<sup>[16,18]</sup> where oxygen vacancies form deep electron traps and can modify barrier heights.<sup>[23,24]</sup> Changes of the charge state of defects in SCRs of BaTiO<sub>3</sub> are particularly expected for transition metal dopants, which exhibit multiple valences.<sup>[13,25]</sup>

In this study, the influence of defects on the Schottky barrier heights at BaTiO<sub>3</sub>/RuO<sub>2</sub> interfaces is reported. The influence of defects will be addressed by two different approaches: 1) intentional acceptor doping and 2) control of the oxygen vacancy concentration. Therefore, intentionally undoped, 0.1 and 0.5 wt% Mn-doped BaTiO<sub>3</sub> ceramics have been synthesized, and the interface formation with RuO<sub>2</sub> electrodes has been studied using PES. The oxygen vacancy concentration and the Mn oxidation state are additionally modified by pre-treatments in oxidizing and reducing atmospheres. Despite the large variation of defect concentrations, no influence of doping and sample pretreatment on the Schottky barrier height is identified. This is related to the high permittivity of BaTiO<sub>3</sub>, which results in wide SCRs even for defect concentrations of 1%. This is confirmed by numerical solutions of the Poisson equation. The effect of the width of the SCRs on the oxygen exchange kinetics at electrode interfaces and for oxygen diffusion in polycrystalline BaTiO<sub>3</sub> will be discussed.

## 2. Sample Preparation and Properties

Intentionally undoped BaTiO<sub>3</sub> and BaTiO<sub>3</sub> doped with up to 0.6 wt% Mn have been fabricated to study the influence of doping and annealing atmosphere on the contact formation to RuO<sub>2</sub> electrodes. The produced samples have the nominal composition of



with  $0 < x < 0.026$  and  $\delta$  depending on the oxygen partial pressure during annealing.

The BaTiO<sub>3</sub> ceramics were synthesized via a conventional solid-state-reaction method. The starting materials were BaCO<sub>3</sub> (99.9% purity), TiO<sub>2</sub> (99.6% purity), and MnCO<sub>3</sub> (99.985% purity) purchased from Thermo Fisher Scientific. The powders were batched stoichiometrically and ball-milled in ethanol for 12 h. After drying, the powders were calcined in a first step at 1100 °C for 5 h in air. Then, the powders were remilled, dried, and sieved, followed by a second calcination in air for 5 h at 1100 °C. X-ray diffraction (XRD) measurements confirmed the main perovskite phase (see Figure S4, Supporting Information). The powders were again sieved, remilled, and dried. The pellets of 0.3 g with 10 mm in diameter were cold-pressed with an isostatic pressure of 350 MPa for 1.5 min (Weber 100 E, Weber, Remshalden, Germany). The pellets were sintered for 6 h at 1350 °C in air. The samples were about 1.1–1.3 mm after sintering and were then ground and polished. The thickness of the measured samples using PES varies from 0.4 to 1.2 mm. The relative densities were measured using the Archimedes method and were found to be 94.5–99% of the theoretical density (see Figure S1, Supporting Information).

The Curie point was determined from temperature-dependent permittivity curves, measured using an LCR meter with a heating rate of 2 K min<sup>-1</sup> for untreated samples (Hewlett Packard 4284A Precision LCR meter, Hewlett Packard Enterprise, USA). For reduced samples, the Curie point was determined from the hysteresis appearing in temperature-dependent conductivity measurements as described in the Supporting Information (see Figure S3, Supporting Information).

For interface studies, the sample surfaces were ground and polished using 1 μm diamond paste finish and lubricant. Samples were then equilibrated at 900 °C for at least 12 h in air with quenching back to RT to ensure the same oxygen vacancy concentration. Reduced samples were additionally annealed at 1100 °C for at least 12 h in 5% H<sub>2</sub>/Ar and quenched to room temperature (RT). The reduced BaTiO<sub>3</sub> samples show a blackish appearance with a conductivity of 10<sup>-1</sup> to 10<sup>-2</sup> S cm<sup>-1</sup>. Oxidized and equilibrated samples are insulating with a conductivity lower than 10<sup>-10</sup> S cm<sup>-1</sup>.

The XRD patterns (see Figure S4, Supporting Information) reveal a pure tetragonal crystal structure for intentionally undoped and 0.05 wt% Mn-doped BaTiO<sub>3</sub>. Additional reflections of a hexagonal phase appear in the patterns of 0.1 and 0.5 wt% Mn-doped BaTiO<sub>3</sub>. Whereas the peak intensities of the hexagonal phase are weak for 0.1 wt%, they are clearly discernable for the 0.5 wt% Mn-doped BaTiO<sub>3</sub>. The coexistence of tetragonal and hexagonal phases for Mn-doping concentrations higher than 0.5% for samples fired in air concurs with literature reports.<sup>[26–28]</sup> The appearance of the hexagonal phase has been related to the oxygen vacancy concentration as well as to the amount of Mn<sup>3+</sup>.<sup>[28]</sup> An appearance of a small hexagonal phase fraction in the XRD pattern of 0.1 wt% Mn-doped BaTiO<sub>3</sub> could indicate a slightly higher Mn<sub>II</sub><sup>3+</sup>/Mn<sub>II</sub><sup>4+</sup> ratio than for the samples reported in the literature.

Temperature-dependent permittivity measurements displayed in Figure 1 indicate that the Curie point  $T_C$  of the untreated

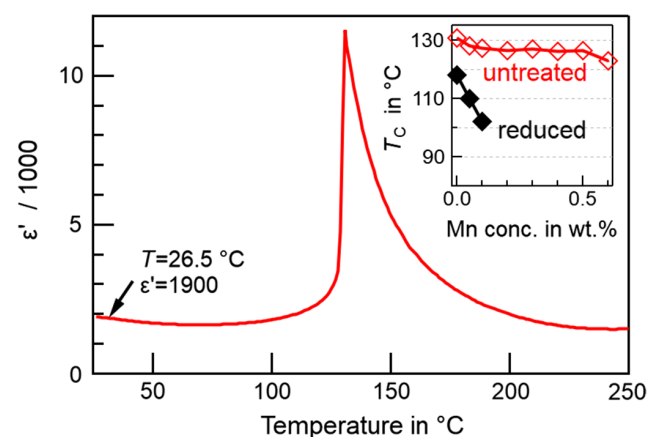


**Figure 1.** Real part of the permittivity as a function of temperature for a frequency of 1000 Hz for an untreated undoped BaTiO<sub>3</sub> ceramic sample. The room temperature permittivity is marked. The inset shows the determined Curie point for a frequency of 1000 Hz determined from the permittivity measurements of untreated samples and from electrical measurements for reduced samples. All samples were measured with Pt electrodes.

samples is only slightly decreasing with increasing Mn-doping concentration for the untreated samples, whereas a strong decrease is observed for the reduced samples. The minor influence of the Mn doping on the Curie point of samples sintered in air is consistent with previous reports and suggests that Mn is present in the  $\text{Mn}^{4+}$  and in the  $\text{Mn}^{3+}$  oxidation states.<sup>[29–31]</sup> The strong decrease in  $T_C$  for the reduced undoped  $\text{BaTiO}_3$  could be attributed to a high charge carrier concentration.<sup>[32]</sup> The Mn-doped samples show an even stronger decrease in the Curie point after reduction, suggesting Mn being mainly in the  $\text{Mn}^{2+}$  oxidation state accompanied by a high oxygen vacancy and electron concentrations.<sup>[29,30,33]</sup> High electrical conductivities of  $10^{-1}$  to  $10^{-2} \text{ S cm}^{-1}$  and a blackish appearance support the assumed high charge carrier concentrations of the reduced samples.

### 3. Surface Properties of Reduced $\text{BaTiO}_3$

This section presents the surface properties of the reduced samples. At the temperatures of  $1100^\circ\text{C}$  used for reduction, cations are mobile and can result in the formation of secondary surface phases,<sup>[10,34,35]</sup> which could affect barrier formation.

X-ray photoelectron spectra reported in this work were recorded using monochromatic Al  $K\alpha$  radiation with a Physical Electronics PHI 5700 spectrometer (Physical Electronics, Chanhassen, MA). Binding energies were calibrated by setting the binding energy of the Fermi edge of a freshly cleaned Ag sample to 0 eV.

Normalized and background subtracted  $\text{Ba } 3d_{5/2}$ ,  $\text{O } 1s$ ,  $\text{Ti } 2p$ , and  $\text{Ba } 4d$  spectra of reduced 0.5 wt% Mn-doped  $\text{BaTiO}_3$  samples before and after the removal of the surface layer by grinding are shown in **Figure 2**. Both Ba peaks exhibit two components indicated by darker (Ba I) and lighter filling (Ba II). This double peak structure of the Ba emissions is well known for  $\text{BaTiO}_3$  and is commonly assigned to a bulk (Ba I) and a surface emission (Ba II).<sup>[36–42]</sup> The intensities of the Ba II components of the ground samples correspond well with those observed for single-crystal  $\text{BaTiO}_3$ . The  $\text{O } 1s$  emission of the ground sample exhibits an asymmetry toward higher binding energies, which is also observed for clean  $\text{BaTiO}_3$  single crystals.<sup>[43]</sup> According to the literature, the O I component is assigned to bulk oxygen, whereas the origin of the asymmetry (O II) is unclear. Here, a possible origin for the latter could be adsorbed oxygen.

The spectra recorded before and after grinding of the surface layer are noticeably different. The high binding energy components of both Ba emissions are significantly higher before the removal of the surface layer. The  $\text{O } 1s$  emission of the non-ground sample is also substantially more broadened toward higher binding energies, indicated by the third component O III. Moreover, the Ba/Ti ratio, obtained from integrated intensities of the  $\text{Ba } 3d_{5/2}$  and  $\text{Ti } 2p$  core levels and spectrometer sensitivity factors,<sup>[44]</sup> differs by almost a factor of 2 and indicates a substantial enrichment of Ba after reduction. Moreover, scanning electron microscopy images reveal small particles at the surface of the reduced samples (see Figure S5, Supporting Information). The particles are estimated to cover less than 10% of total surface area, which is not enough to explain the increased intensity of the Ba II components and of the high binding energy shoulder of the  $\text{O } 1s$  emission. We, therefore, assume

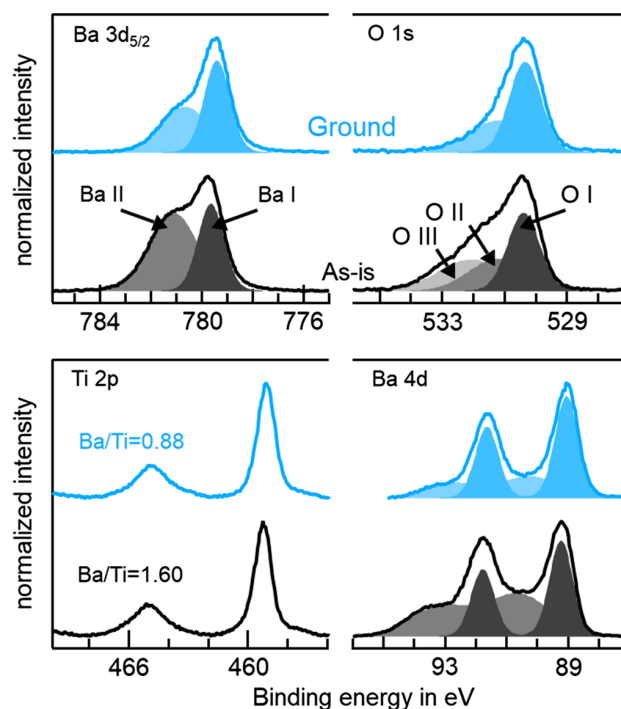


**Figure 2.** Normalized X-ray photoelectron core-level spectra of a reduced 0.5 wt% Mn-doped  $\text{BaTiO}_3$  sample before (black) and after (blue) the removal of the surface layer by grinding. Background subtraction and normalization were performed for better comparison. Curve fitting was conducted for Ba and O emissions using Gauß–Lorentz functions. The derived Ba/Ti ratio calculated with the  $\text{Ba } 3d$  emission is shown for both samples on the right.

that the Ba-rich surface phase is homogeneously covering the reduced surface. This is consistent with the higher intensity of the Ba II component of the  $\text{Ba } 3d_{5/2}$  peak as compared with that of the  $\text{Ba } 4d_{5/2}$  peak, which is related to the higher surface sensitivity of the former. Based on the intensity ratios of the Ba II relative to the Ba I components, the thickness of the Ba-rich surface phase is estimated to be 1–2 nm.

The chemical nature of the surface phase remains unclear. Potential phases, which might occur, are  $\text{BaO}$ ,  $\text{BaCO}_3$ ,  $\text{Ba(OH)}_2$ ,  $\text{BaTi}_2\text{O}_4$ , or Ruddlesden–Popper phases with incorporated additional  $\text{BaO}$  layers. The latter has been observed for  $\text{BaTiO}_3$  thin films.<sup>[45]</sup> In contrast, the solubility of  $\text{BaO}$  in  $\text{BaTiO}_3$  for bulk samples sintered in air has been reported to be below 0.1%.<sup>[46]</sup> Samples with higher  $\text{BaO}$  excess exhibit secondary  $\text{Ba}_2\text{TiO}_4$  phases. A higher solubility for the highly reducing anneal used in this work cannot be excluded, however. The formation of  $\text{Ba(OH)}_2$  and  $\text{BaCO}_3$  is also not likely, as hydroxides are usually not stable at higher temperatures, and the carbon contamination is too low to explain the intensities of the additional Ba and O components of the annealed samples. Also, the binding energy of the carbon peak of  $\approx 285 \text{ eV}$  does not match with a  $\text{BaCO}_3$  phase.<sup>[44]</sup> While the binding energies of the additional Ba and O components would correspond to the formation of  $\text{BaO}$  at the surface, the formation of a  $\text{BaO}$  phase of acceptor-doped material under reducing conditions is unusual, as cation vacancy formation is generally favoured under oxidizing

conditions and for donor-doped material.<sup>[47–51]</sup> Such a behavior is also documented for SrTiO<sub>3</sub><sup>[10,34,52]</sup> and Na<sub>1/2</sub>Bi<sub>1/2</sub>TiO<sub>3</sub>–BaTiO<sub>3</sub>.<sup>[53]</sup>

A possible origin of the formation of the Ba-rich surface phase may be related to the formation of a surface SCR. Oxygen vacancies will have lower formation enthalpies at the surface than in the bulk (see the previous study<sup>[54]</sup>). The higher concentration of oxygen vacancies at the surface leads to a positive surface charge and, consequently, to a downward band bending toward the surface. As the Fermi energy in the bulk of the sample is already close to the conduction band, the surface will become highly degenerate. This is consistent with the very high Fermi energies observed by PES and the formation of Ti<sup>3+</sup> species at the reduced surfaces. The latter is evident from the small peak at low binding energies in the Ti 2*p* spectra in Figure 2. The formation of a degenerate surface is, furthermore, consistent with the observations of 2D electron gases at SrTiO<sub>3</sub> and also at BaTiO<sub>3</sub> surfaces,<sup>[55,56]</sup> which have been assigned to surface oxygen vacancies.

The high Fermi energy at the surface will lower the formation enthalpy of cation vacancies. In agreement between density functional theory calculations<sup>[57,58]</sup> and defect chemical measurements of donor-doped samples,<sup>[47–51]</sup> BaTiO<sub>3</sub> will form B-site (Ti) vacancies rather than A-site (Ba) vacancies. The formation of Ti vacancies will proceed by segregation of Ti to the surface, where it forms TiO<sub>2</sub> particles and leaves behind a Ba-rich surface phase. Such a scenario is consistent with all our experimental observations and with the formation of Ti-rich precipitates in donor-doped BaTiO<sub>3</sub>.<sup>[59]</sup> The resulting surface chemical and electronic structures are shown in Figure 3.

However, a final statement on the composition of the small particles reported in the scanning electron microscopy images of the reduced sample is not possible without further measurements. Here, cross-sectional high-resolution transmission electron microscopy (HRTEM) could be a powerful technique to elucidate the chemical and structural nature of the precipitates.

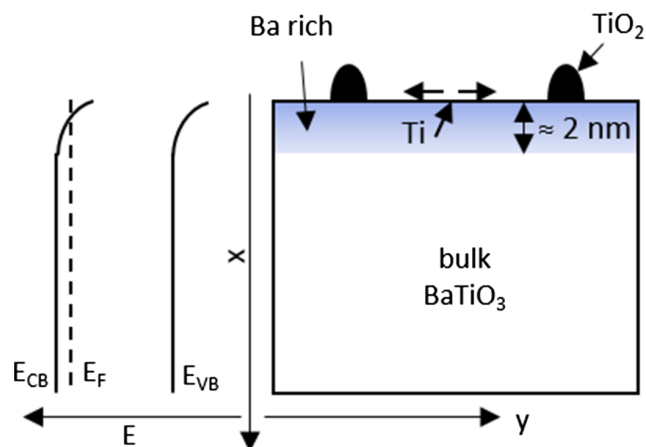


**Figure 3.** Energy band diagram (left) and schematic composition of BaTiO<sub>3</sub> reduced by annealing at 1100 °C in Ar/H<sub>2</sub> (right). Surface oxygen vacancies generate a positively charge surface. As the Fermi energy is already close to the conduction band in the bulk after reduction, a 2D electron gas forms at the surface, which results in the formation of Ti vacancies. The Ti atoms diffuse to the surface, form TiO<sub>2</sub> precipitates, and leave behind a Ba-rich surface phase.

## 4. Interface Analysis

### 4.1. Experimental Procedure

The deposition of the electrode material and the PES analysis were performed in the DArmstadt Integrated SYstem for MATerials research (DAISY-MAT),<sup>[17]</sup> which combines a multi-technique surface analysis system with several deposition chambers using an ultrahigh vacuum sample transfer. Before electrode deposition, reduced samples were cleaned by heating in one of the deposition chambers of the DAISY-MAT system. Cleaning, that is the removal of carbon species from the surface, is more efficient in the presence of oxygen when CO<sub>2</sub> can form.<sup>[60]</sup> However, the addition of oxygen would reoxidize the surface region of the reduced samples. Therefore, reduced samples were heated for at least 1 h at 500 °C in vacuum (10<sup>–8</sup> mbar). In contrast, equilibrated samples were cleaned for at least 1 h at 400 °C in 5 × 10<sup>–3</sup> mbar oxygen. Samples labeled as oxidized were additionally exposed to an oxygen plasma for 15 min at 200 °C using a GenII plasma source (Tetra, Frankfurt, Germany) operating in the atom mode at a pressure of 2.0 × 10<sup>–4</sup> mbar.

In a typical interface experiment, the bare sample surface is measured in a first step. In the present case, PES measurements of the bare surfaces without sample charging are only possible for the reduced samples. The RuO<sub>2</sub> films were deposited by direct current (DC) magnetron sputtering at room temperature with an applied DC-power density of 0.5 W cm<sup>–2</sup>, a gas pressure of 1 × 10<sup>–2</sup> mbar, an Ar/O<sub>2</sub> mixture with 7.5%O<sub>2</sub>, and a target to a sample distance of 9.4 cm. Thin RuO<sub>2</sub> films were deposited until barrier formation is completed. PES measurements were carried out after each deposition step. Charging of the insulating BaTiO<sub>3</sub> samples can be avoided by electrically contacting the sample via the conducting RuO<sub>2</sub> films.

### 4.2. Interface Formation

The upper panel of Figure 4 shows the survey spectra of a reduced, nominally undoped BaTiO<sub>3</sub> ceramic before and after deposition of 5 nm RuO<sub>2</sub>. The survey spectra of the bare surface reveal the typical Ba, Ti, and O emission lines. Small Si, Ca, and C contaminations are detected on the surface of some samples. Deposition of 5 nm RuO<sub>2</sub> results in an attenuated signal of the substrate emissions (Ba and Ti) and the growth of the Ru lines.

The core-level emissions of Ba 3*d*<sub>5/2</sub>, O 1*s*, Ti 2*p*, Ru 3*d*, Ba 4*d*, and the valence bands of the bare BaTiO<sub>3</sub> surface and during stepwise deposition of RuO<sub>2</sub> are shown in the lower panel of Figure 4 from bottom to top. Curve fitting was conducted for all BaTiO<sub>3</sub> emissions of the bare surface. The Ba 3*d*<sub>5/2</sub> and Ba 4*d* core-level spectra are composed of two components, as described in Section 3. The Ti 2*p* spectrum shows a symmetric line shape with a shoulder at lower binding energies, which is attributed to Ti<sup>3+</sup>. The small intensity in the Ru 3*d* spectral region at 285 eV for the bare BaTiO<sub>3</sub> surface originates from some remaining C impurities, which have not been completely removed by the cleaning procedure.

With increasing RuO<sub>2</sub> thickness, the intensity of the Ba and Ti core levels gradually decreases, whereas the intensity of the Ru emission increases. The Ti 2*p* emission is partially superimposed

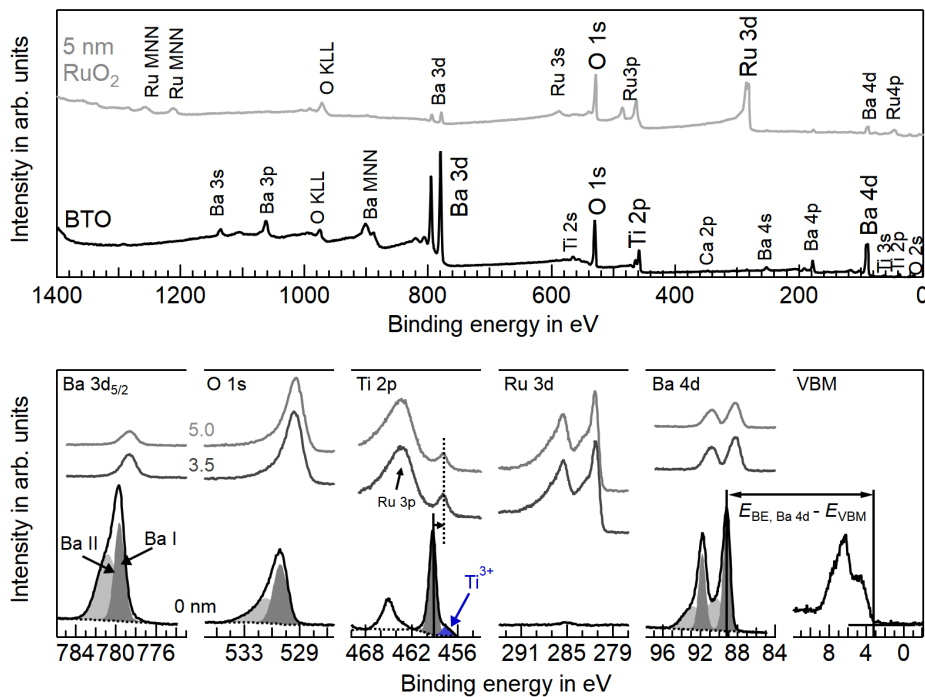


**Figure 4.** X-ray photoelectron survey spectra (upper panel) and core-level/valence band emissions (lower panel) of a reduced undoped BaTiO<sub>3</sub> ceramic recorded with monochromatic Al K $\alpha$  radiation. The RuO<sub>2</sub> electrode thickness is indicated in nanometers. Curve fitting was conducted for all BaTiO<sub>3</sub> emissions using Gauß–Lorentz functions. An example for the core level to VBM distance is given between the Ba 4d peak and the VBM. The binding energy shift before and after contact formation is indicated by the two lines in the Ti 2p spectra.

with the growing Ru 3p emission. Nevertheless, the Ti 2p binding energy can still be determined, as the main Ti 2p<sub>3/2</sub> emission remains well separated. As BaTiO<sub>3</sub> and RuO<sub>2</sub> both contain oxygen, the O emission is not attenuated with increasing RuO<sub>2</sub> thickness. RuO<sub>2</sub> deposition leads to a shift of the Ba and Ti emissions toward lower binding energies, as indicated by the solid and dashed lines in the Ti 2p spectrum.

After RuO<sub>2</sub> deposition, the valence bands of both materials are superimposed, making  $E_F - E_{VBM}$  inaccessible. The core level to valence band distance is a material constant, which can be used to obtain the Fermi level during the interface experiment by subtracting the specific distance from the corresponding core-level binding energies.<sup>[61]</sup> An example of a core level to valence band maximum (VBM) distance determination for the Ba4d emission ( $E_{Ba4d}^{VB} = E_B^{Ba4d} - E_B^{VBM}$ ) is given in Figure 4.

### 4.3. The Barrier Heights

The Fermi energy during the contact formation was derived by subtracting the following core level to VBM distances:  $E_{Ba3d}^{VB} = 776.38$  eV,  $E_{Ti2p}^{VB} = 455.96$  eV, and  $E_{Ba4d}^{VB} = 85.95$  eV. These values correspond to the average distance calculated for all measured bare surfaces of the reduced BaTiO<sub>3</sub> samples. The values for Ba 3d and Ba 4d emissions were obtained using the bulk Ba I components of the 3d<sub>5/2</sub> and 4d<sub>5/2</sub> emissions, whereas the binding energy of the Ti 2p<sub>3/2</sub> was used for the Ti 2p emission. The derived distances are in good agreement with the values of previous studies of BaTiO<sub>3</sub> single crystals.<sup>[40,42]</sup>

The barrier formation by RuO<sub>2</sub> deposition has been studied for undoped, 0.1 and 0.5 wt% Mn-doped BaTiO<sub>3</sub> ceramics in different oxidation states. The Fermi-level positions at the interfaces are derived from the three cation core-level binding energies and are displayed in Figure 4 as a function of RuO<sub>2</sub> thickness. Fermi-level positions for the bare surfaces (0 nm) are only obtained for the reduced (non-charging) samples. The value of  $E_F - E_{VB} = 3.2 \pm 0.05$  eV is close or even inside the conduction band. These high Fermi-level positions also agree with the high conductivity of the reduced samples (conductivities of 0.01 to 0.1 S cm<sup>-1</sup> correspond to electron concentrations of 10<sup>17</sup> – 10<sup>18</sup> cm<sup>-3</sup> for an electron mobility of 0.5 cm<sup>2</sup> Vs<sup>-1</sup>).

The Fermi-level positions obtained after deposition of 3.5 nm RuO<sub>2</sub> are identical to those obtained for a total RuO<sub>2</sub> thickness of 5 nm. This indicates that the barrier is already fully developed at a RuO<sub>2</sub> thickness of 3.5 nm, which agrees with previous studies of the contact formation between dielectric oxides and RuO<sub>2</sub>. The latter indicate that the contact formation is completed at a RuO<sub>2</sub> thickness of 12 nm.<sup>[18,40,62]</sup>

The reduced samples exhibit smaller binding energy shifts for the Ba core levels as compared with shifts of the Ti core levels. The effect is less pronounced but still evident for the sample without the surface layer. This results in an apparent dependence of the Fermi-level position on the core level used for its derivation. An interfacial reaction as origin of the different binding energy shifts is excluded, as the equilibrated and oxidized samples show identical Fermi-level position for all three core levels. Different binding energy shifts of core levels may also occur

when the SCR related to the Schottky barrier formation is very narrow. The core levels with the lowest kinetic energy (highest binding energy) of the photoelectrons should then exhibit the largest shift. In this case, it is expected that the binding energy shifts are largest for Ba 3*d* and smallest for Ba 4*d*, being clearly in contrast with the results shown in Figure 5.

It has recently been demonstrated that the Zn 2*p* core level and Zn LMM Auger emission also exhibit different binding energy shifts during contact formation with RuO<sub>2</sub>.<sup>[18]</sup> In this case, the different shifts can be clearly assigned to a change in the screening of the photoelectron core hole during evolution of the barrier. The origin of this effect could not be finally resolved, but it has been suggested that it is related to the high electric field, which is induced by the large band bending due to the high work function of RuO<sub>2</sub> (see the following discussion). This situation is very similar in the present case, where the Fermi energy at the interface differs by more than 1.2 eV from that in the bulk of the reduced samples (see Section 5). In contrast, the bulk Fermi energy of the equilibrated and oxidized samples should be comparable or even lower than that at the RuO<sub>2</sub> interface. No high electric fields should, therefore, be present at these interfaces. Therefore, the different (comparable) Fermi energies derived from the different core levels, which are observed at the RuO<sub>2</sub> interfaces of reduced (equilibrated and oxidized) BaTiO<sub>3</sub>, are, therefore, consistent with the presence (absence) of a high electric field in the SCR as proposed for the ZnO/RuO<sub>2</sub> interface.<sup>[18]</sup> A change of core hole screening during interface formation is also indicated by the change of the Ba 3*d* and 4*d* line shapes in the course of RuO<sub>2</sub> deposition. In particular, the intensity ratio and energy separation of the Ba I and Ba II composition are changing during

interface formation. Such effects have also been observed at other BaTiO<sub>3</sub> and (Ba,Sr)TiO<sub>3</sub> interfaces.<sup>[63–66]</sup>

The Fermi energies derived from the Ti 2*p* core levels are identical within the experimental uncertainty of ±0.05 eV for the equilibrated, the oxidized, and the reduced sample after the removal of the surface layer. The value of  $E_F - E_{VB} = 1.7 \pm 0.05$  eV is also independent of the Mn dopant concentration. Only the reduced samples exhibit a clearly higher Fermi-level position in contact with RuO<sub>2</sub>. The latter is attributed to the Ba-rich surface phase.

The Fermi-level position at the BaTiO<sub>3</sub>/RuO<sub>2</sub> interface corresponds a Schottky barrier height for the electrons of  $\Phi_{B,n} = 3.1 - 1.7 = 1.4$  eV, where 3.1 eV is taken for the bandgap of BaTiO<sub>3</sub>.<sup>[25]</sup> Such high Schottky barriers are reasonable, considering the effective work function of RuO<sub>2</sub> of 5.6 eV (see discussion in the previous study<sup>[67]</sup>). The barrier heights are comparable to that obtained at BaTiO<sub>3</sub>/NiO interfaces,<sup>[43]</sup> which has been the highest reported barrier height for BaTiO<sub>3</sub>. Slightly lower barrier heights of 1.85 eV have been reported for SrTiO<sub>3</sub>/RuO<sub>2</sub> interfaces.<sup>[14]</sup> In the case of ZnO, Schottky barrier heights at RuO<sub>2</sub> contacts are also among the highest reported for this material.<sup>[18]</sup>

The independence of barrier height on doping concentration and oxidation state of the sample is surprising. For such high defect concentrations, one has to expect the formation of rather narrow SCRs, which should result in an effective modification of the barrier height.<sup>[14,17]</sup> This observation is addressed in the following section.

## 5. Simulation of the SCR

To calculate the space-charge potential  $\phi$  for the given interface between BaTiO<sub>3</sub> and RuO<sub>2</sub>, the Poisson equation needs to be solved

$$\frac{\partial^2 \phi}{\partial x^2} = -\frac{\rho(x)}{\epsilon \epsilon_0} \quad (2)$$

Here,  $\epsilon$  is the material's permittivity,  $\epsilon_0$  is the vacuum permittivity, and  $\phi$  is the charge density, which includes all electronic and ionic charges.

The defect chemistry of acceptor-doped BaTiO<sub>3</sub> is excessively described in the literature.<sup>[13,25,47–51,57,58,68–70]</sup> The relevant defect reactions for Mn-doped BaTiO<sub>3</sub> are the oxygen exchange reaction, the electron–hole pair reaction, and the acceptor ionization reactions



According to defect calculations of BaTiO<sub>3</sub>,<sup>[57,58]</sup> only doubly charged oxygen vacancies are considered. The corresponding charge density for Mn-doped BaTiO<sub>3</sub> is given by

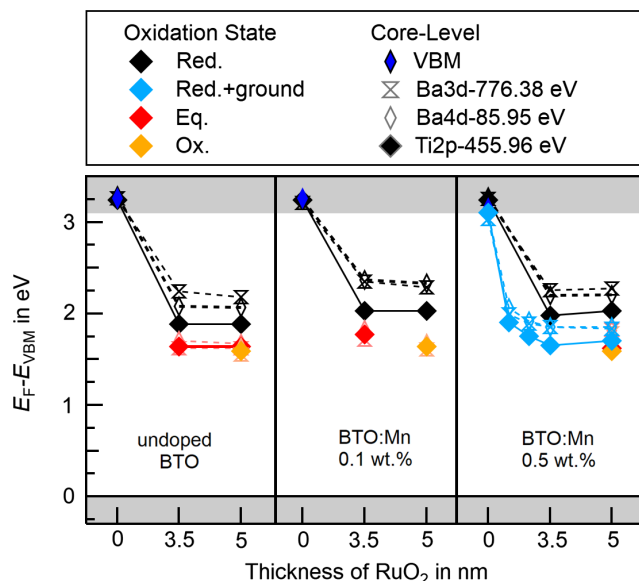


**Figure 5.** Evolution of VBM binding energy  $E_F - E_{VBM}$  with increasing RuO<sub>2</sub> thickness for undoped, 0.1 and 0.5 wt.% Mn-doped BaTiO<sub>3</sub> ceramics in an oxidized (orange), equilibrated (red), and reduced state (black). The interface of a reduced 0.5 wt.% Mn-doped sample after the removal of the surface layer is also included (blue). Dashed lines connect values derived from the Ba 3*d* and 4*d* emissions and solid lines to those from Ti 2*p* emissions.

$$\rho = p - n + 2N_{V_O} - 2N_{Mn''_{Ti}} - N_{Mn'_{Ti}} \quad (7)$$

The concentrations of holes  $h$ , electrons  $e$ , doubly charged oxygen vacancies  $V_O^{\bullet\bullet}$ , and singly and doubly charged Mn dopants  $Mn'_{Ti}/Mn''_{Ti}$  depend on the Fermi level and were calculated according to Equation (S1)–(S5), Supporting Information.

The entire procedure has been implemented in MATLAB and has been solved using the boundary value problem solver of the fifth-order method (bvp5c).<sup>[71]</sup> For the model, all ionic defects are assumed to be immobile, which is reasonable, as RuO<sub>2</sub> has been deposited at room temperature. The boundary conditions are set as follows: flat band potential in the bulk ( $\phi'(x = \infty) = 0$ ) and the experimental determined value for the Schottky barrier height for electrons  $\Phi_{B,n}$  as interface potential ( $\phi(x = 0) = \Phi_{B,n}$ ).

The simulations shown in **Figure 6** have been conducted for a 0.5 wt% Mn-doped sample, corresponding to an acceptor concentration of  $N_{Mn} = 3.30 \times 10^{20} \text{ cm}^{-3}$ . Three different values of oxygen vacancy concentration have been applied. To

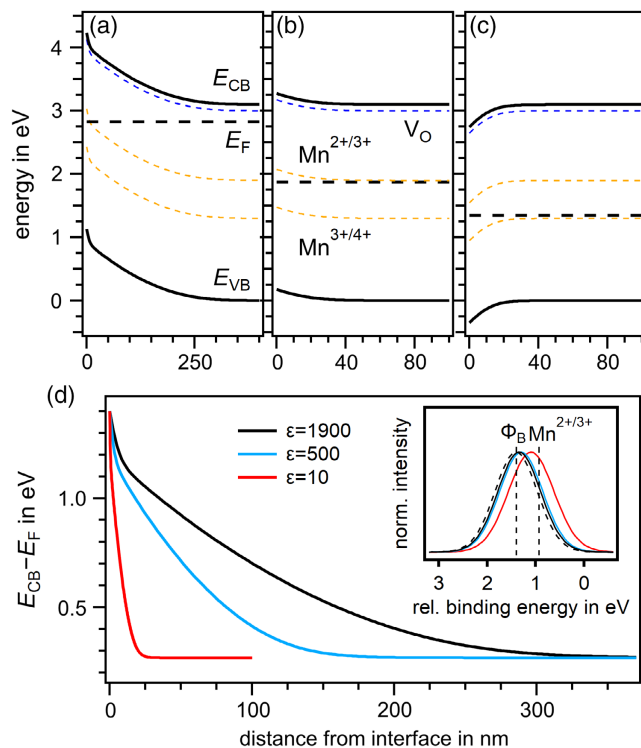


**Figure 6.** Simulated energy band diagrams BaTiO<sub>3</sub> doped with  $3.3 \times 10^{20} \text{ cm}^{-3}$  Mn. The concentrations of oxygen vacancies are a)  $3.31 \times 10^{20} \text{ cm}^{-3}$ , b)  $1.8 \times 10^{20} \text{ cm}^{-3}$ , and c)  $1.0 \times 10^{20} \text{ cm}^{-3}$ , respectively. Other parameters for the simulation are given in the text. The energy is referenced to the VBM positions in the bulk. d) The variation of the conduction band energy  $E_{CB}$  for the conditions given in (a) but for different relative permittivities  $\epsilon$  is shown. Simulated core-level spectra are shown in the insert of (d). Here, the dashed gray spectrum corresponds to a Gaussian peak with a full width at half maximum of 1 eV for a flat potential with  $E_{CB} = 1.4 \text{ eV}$ . The black, blue, and red spectra correspond to the spectra induced by the potential profiles shown in (d) for an inelastic mean free path of the photoelectrons of 2 nm. The two dashed vertical lines in the insert correspond to the position of the Fermi energy at the interface and to that of the  $Mn^{2+/3+}$  charge transition level assumed in the simulations.

simulate reducing conditions, an oxygen vacancy concentration of  $3.31 \times 10^{20} \text{ cm}^{-3}$  has been assumed in Figure 5a, which should result in an electron concentration of  $n \approx 10^{18} \text{ cm}^{-3}$ . For the simulations shown in Figure 5b,c, oxygen vacancy concentrations of 1.8 and  $1.0 \times 10^{20} \text{ cm}^{-3}$  have been used. The three different concentrations result in bulk Fermi energies close to the conduction band (Figure 5a) and close to the  $Mn^{2+/3+}$  transition (Figure 5b) and close to the  $Mn^{3+/4+}$  transition (Figure 5c), respectively.

In the case of the reduced sample, the overall band bending toward the RuO<sub>2</sub> electrode exceeds 1.1 eV. Due to the strong band bending, which is a result of the high Schottky barrier, the  $Mn^{2+/3+}$  charge transition level is crossing the Fermi energy in the SCR. This is noticeable by a change of curvature of the energy bands, which is induced by the strong increase in the effective charge density from  $10^{18}$  to  $3.31 \times 10^{20} \text{ cm}^{-3}$ . Nevertheless, the steeper part of the potential profile still extends over  $\approx 10 \text{ nm}$ , which is better visible from the black curve in Figure 5d. As this is considerably larger than the inelastic mean free path of the photoelectrons of  $\approx 2 \text{ nm}$ , the binding energy of the core levels still represents mostly the potential close to the interface.

To quantify the influence of the change of the Mn oxidation state on the binding energy of the core-level emissions, simulations of spectra profiles have been carried out, assuming a Gaussian peak with a full width at half maximum of 1 eV and an inelastic mean free path of the photoelectrons of 2 nm. More details about the nature of such calculations and their application can be found in the previous studies.<sup>[14,21,22]</sup> The result of the simulations is shown in the insert of Figure 5d. The solid black line, which corresponds to the spectrum calculated to the potential profile indicated by the black line in Figure 5d, is barely shifted from the spectrum obtained for an infinite width of the SCR (dashed curve), whose peak position is indicated in the insert of Figure 5d by  $\phi_B$ . Three simulations have been carried out using the same defect concentrations and energy levels but different relative dielectric permittivities of  $\epsilon = 1900$ , 500, and 10. The corresponding potential profiles and calculated photoelectron spectra are shown by the black, blue, and red curves in Figure 5d, respectively. The value of 1900 corresponds to the value measured at room temperature. As expected from the Poisson equation, the width of the SCR narrows considerably upon reduction of permittivity. Reducing  $\epsilon$  from 1900 to 500 does not lead to a pronounced peak shift. However, the maximum of the peak is shifted by almost 0.4 eV for the lowest permittivity of  $\epsilon = 10$  and becomes close to the position expected for a Fermi energy pinned at the  $Mn^{2+/3+}$  transition. The simulations indicate that the missing dependence of Schottky barrier height at the BaTiO<sub>3</sub>/RuO<sub>2</sub> interface on doping is related to the high permittivity of the sample. Due to its lower relative permittivity, BaSnO<sub>3</sub> might be an interesting host material to study the experimental accessibility of defect energy levels using PES.<sup>[72]</sup>

Accordingly, the introduction of defects in low and high permittivity materials does not have the same influence on the SCR width, which is much larger for high permittivity materials. On the one hand, this will have consequences for the oxygen surface kinetics, where surface SCRs can reduce oxygen incorporation.<sup>[10]</sup> On the other hand, the width of the SCRs will impact the electrical

properties of grain boundaries. Grain boundaries in (acceptor-doped) BaTiO<sub>3</sub> are expected to have a positive grain boundary core charge with an oxygen vacancy depleted SCR.<sup>[10,12,73]</sup> Thus, the oxygen diffusion is suppressed in the SCR compared with the bulk, whereas electronic conduction could be enhanced. Consequently, the impact of grain boundaries on the oxygen diffusion/electronic properties will be more pronounced for high permittivity materials than for low permittivity materials.

## 6. Conclusion

Intentionally undoped and Mn-doped BaTiO<sub>3</sub> ceramic samples have been synthesized by the solid-state processing method. XRD analysis, density determination via the Archimedes method, and temperature-dependent permittivity measurements confirmed the high quality of the samples.

Interface experiments to RuO<sub>2</sub> electrodes have been conducted for undoped, 0.1 and 0.5 wt% Mn-doped samples in oxidized, equilibrated, and reduced states. A barium-rich surface was observed after reduction, which could be removed by grinding and polishing. All samples without Ba-rich surface phase exhibit the same Fermi level of  $E_F - E_{VBM} = 1.7$  eV at the interface with RuO<sub>2</sub>, independent of the Mn content and oxygen vacancy concentration. The Fermi level corresponds to a Schottky barrier height for electrons of  $\Phi_B = 1.4$  eV, which are comparable to the highest measured barrier height for BaTiO<sub>3</sub>.<sup>[43]</sup>

The simulation of the contact formation between Mn-doped BaTiO<sub>3</sub> and RuO<sub>2</sub> confirmed a pronounced influence of permittivity on the width of the SCR. Even for the highest studied defect concentrations, the width of SCRs remains larger than the inelastic mean free path of the photoelectrons. This proves that the measured binding energies correspond to the Fermi level right at the interface and explains why no pinning of the Fermi energy at the defect energy level of Mn could be observed with the current setting. The experimental assessment of defect energy levels, which is, in principle, possible by PES, would require either substantially higher doping levels, materials with lower permittivity, or higher photon energies. The latter will result in higher inelastic mean free paths of the photoelectrons.

The results indicate that the influence of defects on the SCRs will strongly depend on the permittivity of the material. An impact of oxygen surface exchange on ionic and electronic conduction in polycrystalline high permittivity dielectrics has to be expected. Both effects should contribute to the resistance degradation of these materials.

## Supporting Information

Supporting Information is available from the Wiley Online Library or from the author.

## Acknowledgements

This work was supported by the US Air Force of Scientific Research under contract number FA9550-18-1-0385 and by the LOEWE program of the state of Hessen, Germany, within the project FLAME. They also appreciate discussion with Roger A. De Souza and Till Frömling.

Open access funding enabled and organized by Projekt DEAL.

## Conflict of Interest

The authors declare no conflict of interest.

## Data Availability Statement

Research data are not shared.

## Keywords

BaTiO<sub>3</sub>, defects, Schottky barriers

Received: March 15, 2021

Revised: May 7, 2021

Published online: June 7, 2021

- [1] H. Kishi, Y. Mizuno, H. Chazono, *Jpn. J. Appl. Phys.* **2003**, *42*, 1.
- [2] J. Rödel, G. Tomand, *J. Mater. Sci.* **1984**, *19*, 3515.
- [3] T. Baiatu, R. Waser, K. H. Härdtl, *J. Am. Ceram. Soc.* **1990**, *73*, 1663.
- [4] S. Rodewald, N. Sakai, K. Yamaji, H. Yokokawa, J. Fleig, J. Maier, *J. Electroceram.* **2001**, *7*, 95.
- [5] S. H. Yoon, C. A. Randall, K. H. Hur, *J. Appl. Phys.* **2010**, *108*, 064101.
- [6] M. Wojtyniak, K. Szot, R. Wrzalik, C. Rodenbücher, G. Roth, R. Waser, *J. Appl. Phys.* **2013**, *113*, 083713.
- [7] J. J. Wang, H. B. Huang, T. J. M. Bayer, A. Moballeggh, Y. Cao, A. Klein, E. C. Dickey, D. L. Irving, C. A. Randall, L. Q. Chen, *Acta Mater.* **2016**, *108*, 229.
- [8] T. J. M. Bayer, J. J. Carter, J. J. Wang, A. Klein, L. Q. Chen, C. A. Randall, *J. Appl. Phys.* **2017**, *122*, 244101.
- [9] R. A. De Souza, M. Martin, *Phys. Chem. Chem. Phys.* **2008**, *10*, 2356.
- [10] R. A. De Souza, *Adv. Funct. Mater.* **2015**, *25*, 6326.
- [11] J. Maier, *Prog. Solid-State Chem.* **1995**, *23*, 171.
- [12] M. Kessel, R. A. De Souza, M. Martin, *Phys. Chem. Chem. Phys.* **2015**, *17*, 12587.
- [13] R. A. Maier, C. A. Randall, *J. Am. Ceram. Soc.* **2016**, *99*, 3360.
- [14] R. Giesecke, R. Hertwig, T. J. M. Bayer, C. A. Randall, A. Klein, *J. Am. Ceram. Soc.* **2017**, *100*, 4590.
- [15] A. Klein, *J. Phys.: Cond. Matter* **2015**, *27*, 134201.
- [16] S. Siol, J. C. Hellmann, S. D. Tilley, M. Graetzel, J. Morasch, J. Deuermeier, W. Jaegermann, A. Klein, *ACS Appl. Mater. Interfaces* **2016**, *8*, 21824.
- [17] A. Klein, *J. Am. Ceram. Soc.* **2016**, *99*, 369.
- [18] P. Wendel, S. Periyannan, W. Jaegermann, A. Klein, *Phys. Rev. Mater.* **2020**, *4*, 084604.
- [19] S. M. Sze, K. K. Ng, *Physics of Semiconductor Devices*, John Wiley & Sons, Hoboken, NJ **2007**.
- [20] S. Tanuma, C. J. Powell, D. R. Penn, *Surf. Sci.* **1987**, *192*, L849.
- [21] S. Hirose, H. Okushi, S. Ueda, H. Yoshikawa, Y. Adachi, A. Ando, T. Ohsawa, H. Haneda, N. Ohashi, *Appl. Phys. Lett.* **2015**, *106*, 191602.
- [22] A. F. Zurhelle, X. Tong, A. Klein, D. S. Mebane, R. A. D. Souza, *Angew. Chem., Int. Ed.* **2017**, *56*, 14516.
- [23] P. Ágoston, K. Albe, R. M. Nieminen, M. J. Puska, *Phys. Rev. Lett.* **2009**, *103*, 245501.
- [24] M. W. Allen, S. M. Durbin, *Appl. Phys. Lett.* **2008**, *92*, 122110.
- [25] B. A. Wechsler, M. B. Klein, *J. Opt. Soc. Am. B* **1988**, *5*, 1711.
- [26] A. Kirianov, N. Ozaki, H. Ohsato, N. Kohzu, H. Kishi, *Jpn. J. Appl. Phys.* **2001**, *40*, 5619.



- [27] S. Jayanthi, T. R. N. Kutty, *J. Mater. Sci.: Mater. Electron.* **2008**, *19*, 615.
- [28] H. T. Langhammer, T. Müller, K. H. Felgner, H. P. Abicht, *J. Am. Ceram. Soc.* **2000**, *83*, 605.
- [29] H. J. Hagemann, H. Ihrig, *Phys. Rev. B* **1979**, *20*, 3871.
- [30] K. Albertsen, D. Hennings, O. Steigelmann, *J. Electroceramics* **1998**, *2*, 193.
- [31] S. B. Desu, E. C. Subbarao, *Ferroelectrics* **1981**, *37*, 665.
- [32] K. H. Härdtl, R. Wernicke, *Solid State Commun.* **1972**, *10*, 153.
- [33] P. V. Lambeck, G. H. Jonker, *J. Phys. Chem. Solids* **1986**, *47*, 453.
- [34] R. Meyer, A. F. Zurhelle, R. A. D. Souza, R. Waser, F. Gunkel, *Phys. Rev. B* **2016**, *94*, 115408.
- [35] D. M. Long, B. Cai, J. N. Baker, P. C. Bowes, T. J. M. Bayer, J. J. Wang, R. Wang, L. Q. Chen, C. Randall, D. L. Irving, E. C. Dickey, *J. Am. Ceram. Soc.* **2019**, *102*, 3567.
- [36] L. T. Hudson, R. L. Kurtz, S. W. Robey, D. Temple, R. L. Stockbauer, *Phys. Rev. B* **1993**, *47*(16), 10832.
- [37] S. M. Mukhopadhyay, T. C. S. Chen, *J. Mater. Res.* **1995**, *10*, 1502.
- [38] C. Miot, E. Husson, C. Proust, R. Erre, J. P. Coutures, *J. Eur. Ceram. Soc.* **1998**, *18*, 339.
- [39] J. D. Baniecki, M. Ishii, T. Shioga, K. Kurihara, S. Miyahara, *Appl. Phys. Lett.* **2006**, *89*, 162908.
- [40] F. Chen, A. Klein, *Phys. Rev. B* **2012**, *86*, 094105.
- [41] J. E. Rault, G. Agnus, T. Maroutian, V. Pillard, P. Lecoeur, G. Niu, B. Vilquin, M. G. Silly, A. Bendounan, F. Sirotti, N. Barrett, *Phys. Rev. B* **2013**, *87*, 155146.
- [42] A. H. Hubmann, S. Li, S. Zhukov, H. Von Seggern, A. Klein, *J. Phys. D: Appl. Phys.* **2016**, *49*, 295304.
- [43] D. M. Long, A. Klein, E. C. Dickey, *Appl. Surf. Sci.* **2019**, *466*, 472.
- [44] J. F. Moulder, W. F. Stickle, P. E. Sobol, K. D. Bomben, *Handbook of X-ray Photoelectron Spectroscopy*, Physical Electronics, Inc., Eden Prairie **1995**.
- [45] T. Suzuki, Y. Nishi, M. Fujimoto, *J. Am. Ceram. Soc.* **2000**, *83*, 3185.
- [46] Y. H. Hu, M. P. Harmer, D. M. Smyth, *J. Am. Ceram. Soc.* **1985**, *68*, 372.
- [47] N. H. Chan, D. M. Smyth, *J. Am. Ceram. Soc.* **1984**, *67*, 285.
- [48] F. D. Morrison, A. M. Coats, D. C. Sinclair, A. R. West, *J. Electroceram.* **2001**, *6*, 219.
- [49] D. M. Smyth, *J. Electroceramics* **2002**, *9*, 179.
- [50] H. I. Yoo, C. R. Song, D. K. Lee, *J. Electroceramics* **2002**, *8*, 5.
- [51] D. M. Smyth, *J. Electroceram.* **2003**, *11*, 89.
- [52] K. Szot, W. Speier, U. Breuer, R. Meyer, J. Szade, R. Waser, *Surf. Sci.* **2000**, *460*, 112.
- [53] P. Ren, M. Gehringer, B. Huang, A. P. Hoang, S. Steiner, A. Klein, T. Frömling, *J. Mater. Chem. C* **2021** <https://doi.org/10.1039/d0tc05728b>.
- [54] S. Lany, A. Zakutayev, T. O. Mason, J. F. Wager, K. R. Poepplmeier, J. D. Perkins, J. J. Berry, D. S. Ginley, A. Zunger, *Phys. Rev. Lett.* **2012**, *108*, 016802.
- [55] A. F. Santander-Syro, O. Copie, T. Kondo, F. Fortuna, S. Pailhès, R. Weht, X. G. Qiu, F. Bertran, A. Nicolaou, A. Taleb-Ibrahimi, P. L. Fèvre, G. Herranz, M. Bibes, N. Reyren, Y. Apertet, P. Lecoeur, A. Barthélémy, M. J. Rozenberg, *Nature* **2011**, *469*, 189.
- [56] T. C. Rödel, F. Fortuna, S. Sengupta, E. Frantzeskakis, P. L. Fèvre, F. Bertran, B. Mercey, S. Matzen, G. Agnus, T. Maroutian, P. Lecoeur, A. F. Santander-Syro, *Adv. Mater.* **2016**, *28*, 1976.
- [57] P. Erhart, K. Albe, *J. Appl. Phys.* **2007**, *102*, 084111.
- [58] J. N. Baker, P. C. Bowes, J. S. Harris, D. L. Irving, *J. Appl. Phys.* **2018**, *124*(11), 114101.
- [59] T. Frömling, J. Hou, W. Preis, W. Sitte, H. Hutter, J. Fleig, *J. Appl. Phys.* **2011**, *110*, 043531.
- [60] Y. Gassenbauer, R. Schafraneck, A. Klein, S. Zafeiratos, M. Hävecker, A. Knop-Gericke, R. Schlögl, *Phys. Rev. B* **2006**, *73*, 245312.
- [61] E. A. Kraut, R. W. Grant, J. R. Waldrop, S. P. Kowalczyk, *Phys. Rev. B* **1983**, *28*, 1965.
- [62] R. Schafraneck, J. Schaffner, A. Klein, *J. Eur. Ceram. Soc.* **2010**, *30*, 187.
- [63] R. Schafraneck, S. Payan, M. Maglione, A. Klein, *Phys. Rev. B* **2008**, *77*, 195310.
- [64] S. Balaz, Z. Zeng, L. J. Brillson, *J. Appl. Phys.* **2013**, *114*, 183701.
- [65] S. Li, A. Wachau, R. Schafraneck, A. Klein, Y. Zheng, R. Jakoby, *J. Appl. Phys.* **2010**, *108*, 014113.
- [66] S. Li, C. Ghinea, T. J. M. Bayer, M. Motzko, R. Schafraneck, A. Klein, *J. Phys.: Cond. Matter* **2011**, *23*, 334202.
- [67] Y. Hermans, A. Klein, K. Ellmer, R. van de Krol, T. Toupance, W. Jaegermann, *J. Phys. Chem. C* **2018**, *122*, 20861.
- [68] H. J. Hagemann, D. Hennings, *J. Am. Ceram. Soc.* **1981**, *64*, 590.
- [69] R. N. Schwartz, B. A. Wechsler, *Phys. Rev. B* **1993**, *48*, 7057.
- [70] I. Suzuki, L. Gura, A. Klein, *Phys. Chem. Chem. Phys.* **2019**, *21*, 6238.
- [71] MATLAB, version 9.7.0.1190202 (R2019b), The MathWorks Inc., Natick, MA **2019**.
- [72] É. Bévilion, A. Chesnaud, Y. Wang, G. Dezanneau, G. Geneste, *J. Phys.: Cond. Matter* **2008**, *20*, 145217.
- [73] R. Waser, R. Hagenbeck, *Acta Mater.* **2000**, *48*, 797.